In silico framework to inform the design of repair constructs for peripheral nerve injury repair

S.Laranjeira[1,3],G. Pellegrino[1], K.S. Bhangra[2,3], J.B. Phillips[2,3], R.J. Shipley[1,3]

[1] UCL Mechanical Engineering, London, UK, [2] Department of Pharmacology, UCL School of Pharmacy, London, UK., [3] UCL Centre for Nerve Engineering, UK.

Abstract

Peripheral nerve injury is debilitating, causing loss of sensation and muscle control, chronic pain and disability. Transected nerves have the potential to regenerate following surgical repair, but there are serious limitations for injury sites where there are gaps as regeneration requires a supportive microenvironment. The clinical gold standard is to bridge the severed nerve ends with a nerve autograft harvested from another part of the patient's body; however, donor site morbidity, limited availability and poor outcomes mean there is a clear need to develop alternatives.

Advances in tissue engineering together with stem cell technologies provide promising routes for engineering living artificial nerve replacement tissues, but progress is hampered due in part to a lack of consensus on how to arrange materials and cells in space to maximize nerve regeneration. This is compounded by a reliance on experimental testing, which precludes extensive investigations of multiple parameters due to time and cost limitations.

Here, a computational model is developed and solved to simulate growth of repairing peripheral nerve neurites. This model is parameterised against available literature data from a range of experimental setups, to provide a predictive tool to inform the design of engineered replacement tissues for peripheral nerve injury repair. The *in silico* framework is explored in a case study to inform the design of an engineered repair construct. This case study focuses on a construct comprised of collagen hydrogel with embedded synthetic biomaterial fibres to promote neurite growth through the provision of mechanical and directional cues. A particle swarm optimisation algorithm, implemented through parallel computing, is deployed to optimise the size and the number of fibres needed to maximize the rate of neurite regrowth; robustness of the predictions is explored through an extensive sensitivity analysis, and new design strategies are identified. The approach provides an *in silico* tool to inform the design of engineered replacement tissues, with opportunity for further development to multi-cue environments and validation testing.

1 Introduction

Peripheral nerve injuries affect 1 M people p.a. in Europe and the US (1). In the most severe cases, when nerves are severed, patients experience disability and long-term neuropathic pain. The current gold-standard treatment for these patients is surgery where the gap is repaired by grafting a healthy section of nerve (nerve autograft) taken from elsewhere within the patient. Several limitations have been associated with this treatment including the limited availability of healthy nerve, morbidity at the site of the donor nerve, and limited functional recovery. For example, Ruijs *et al*. (2) performed a meta-analysis of patients with nerve injuries and observed that only around 50% of patients with nerve autografts experienced meaningful functional recovery.

These considerations have motivated research to develop alternatives to grafting by engineering nerve repair construct (NRCs) to provide mechanical and chemical cues that promote and guide nerve growth. An NRC consists of a sheath containing materials and therapeutic cells, sutured into the gap between nerve stumps at the injury site (Fig. 1). Many designs have been developed and some have been FDA approved; however, very few have been translated into clinical practice (3,4). Pedrosa *et al*. (4) summarises the breadth of components that have been explored to engineer a regenerative microenvironment, including material scaffolds, topographical patterning, therapeutic cells, soluble factors, *etc* (see Fig. 1). Each of these components requires a number of design choices, e.g. 70 different biomaterial options that have been proposed for repair scaffolds (5). In addition,, the spatial organisation of material requires careful consideration to exploit neurite responses to their local environment. Given the logistical and financial constraints of experimental investigation, we propose a computational models of peripheral nerve regeneration to inform the design of novel NRCs.

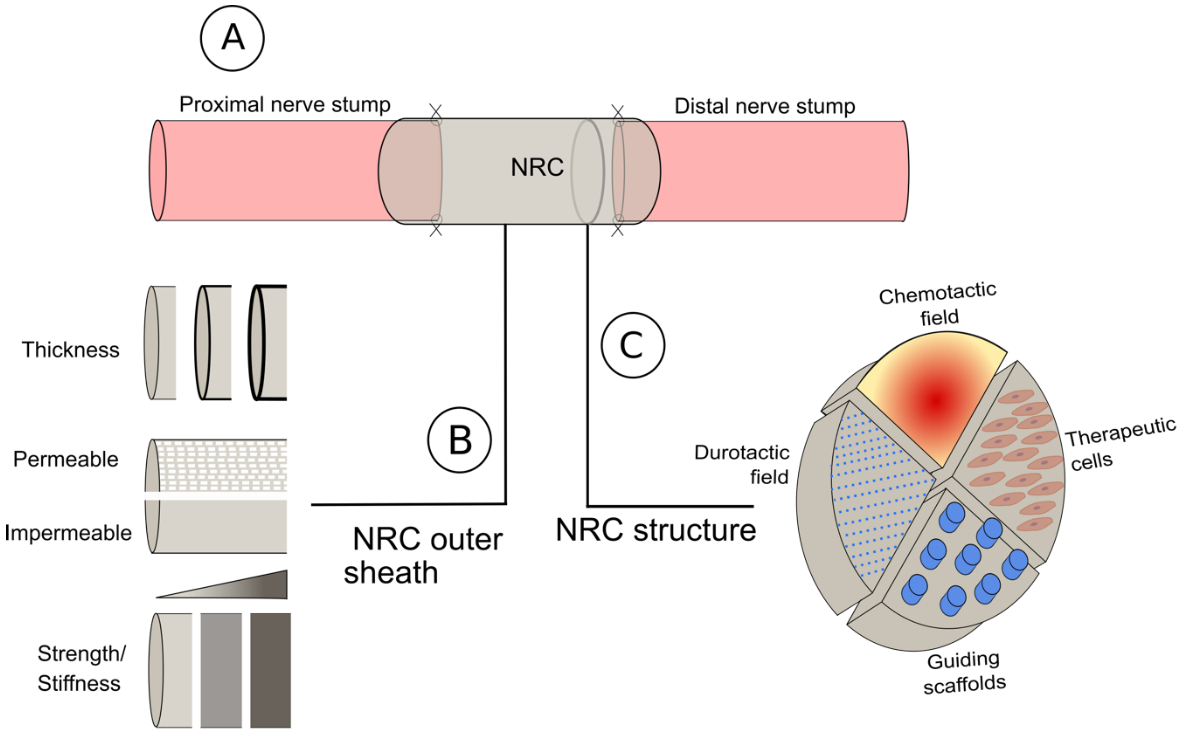

Fig. 1: Schematic demonstrating some of the options available when designing an NRC.
Schematic of (A) the positioning of nerve repair constructs (NRCs), and the design choices when engineering an NRC. These include parameters that define (B) the outer sheaths thickness, strength/stiffness and permeability as well as (C) the core material that may include scaffolds, therapeutic cells and durotactic and chemotactic gradients, whose spatial distribution needs to be carefully considered.

Several computational models have been developed to simulate the growth of neurites in response to chemical cues (6–11), including through a peripheral NRC (10,11) . These models have provided valuable insights into how chemical factors influence neurite growth; however, they are limited to one spatial dimension, and do not explore the role of materials and physical factors in determining neurite growth and guidance. Here we develop a framework based on a discrete random walk, which is capable of describing neurite responses to a range of different cues, in a 3D environment that mimics the architecture of an NRC. Although the framework we propose is generic and could be applied in numerous contexts, here we focus on the role that material and physical cues play in determining the rate of neurite growth. Given the goal to use the model to inform the design of NRCs, it is essential that the computational framework can simulate a realistic repair setting, including the growth of thousands of neurites over a time period of weeks. Furthermore, we take particular care to parameterise and validate the predictions of the model against experimental data, and test the sensitivity of the model to perturbations in its defining parameters.

The potential of this framework is explored by applying it to a specific NRC design - a cellular, collagen-based hydrogel with embedded stiff fibres, as depicted in Fig. 2. Collagen is a promising hydrogel base for NRCs (4,12,13), and when combined with self-aligned therapeutic cells to form an artificial tissue has been shown to support comparable levels of nerve regeneration to nerve grafts in preclinical studies (12,14). One option for augmenting this regeneration is by embedding stiff material fibres in the hydrogel base, to provide an additional stiffness and directional cue to guide and accelerate neurite growth. Here we focus on the example of phosphate glass fibres (PGFs), which have been shown *in vivo* to promote growth (15). We focus on the geometry of a rat sciatic nerve injury repair, as it is commonly used for testing of nerve injury repair strategies. The *in silico* framework to test the balance between providing directional cues for regeneration by embedding fibred, whilst not limiting space availability and blocking the growth of neurites. Through a particle swarm optimisation (PSO) algorithm, we identify the number and size of fibres that maximise the number of neurites that reach the distal end of the NRC within 8 weeks (a typical repair testing timeframe). In this way, we demonstrate how to build an *in silico* framework tailored to available experimental data, and use it to make predictions that can inform future experimental work.

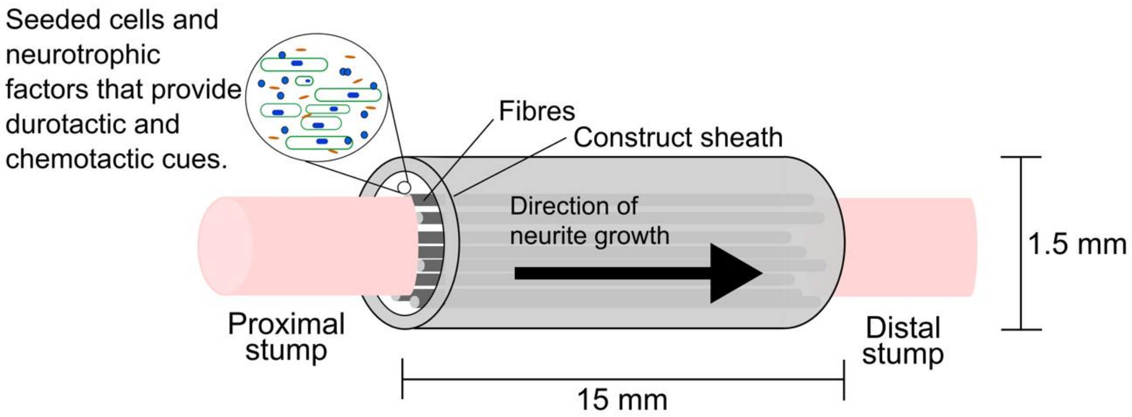
Seeded cells and neurotrophic factors that provide durotactic and chemotactic cues.
Fibres
Construct sheath
Direction of neurite growth
1.5 mm
Proximal stump
Distal stump
15 mm

Fig. 2: Example NRC fabricated from a collagen-based hydrogel with embedded stiff fibres .
A typical NRC geometry and composition for pre-clinical studies in a rat sciatic nerve injury model. The NRC bridges the proximal and distal stumps, and consists of a collagen hydrogel with embedded PGFs, surrounded by an outer biomaterial sheath. Typical dimensions for a rat sciatic nerve injury repair are indicated.

2 Methods

The framework developed describes the growth of neurites in an NRC, consisting of two key components: 1. the meshing of an NRC geometry to provide the geometrical substrate for the computational model, 2. the random walk-based model for simulating the growth of neurites. In each case, we describe the general form of the mesh or model, and then its implementation for the case study to explore embedding PGFs in a collagen-based NRC to maximise neurite growth.

2.1 Geometrical Meshing of an Engineered NRC

The model is solved on a cylindrical geometry representative of an NRC using software COMSOL Multiphysics (*COMSOL Multiphysics® v. 3.5. www.comsol.com. COMSOL AB, Stockholm, Sweden*). This software is able to capture complex geometries described through sophisticated meshes, as well as both discrete and continuous model descriptions. In the long-term, this will enable the extension of the framework described here to account for chemotactic and cellular factors (16), as well as the physical and material-based cues here demonstrated.

Here we describe the generation of numerical lattices for simulating growth of neurites using a random walk model, in an NRC. A typical engineered NRC for use in a rat sciatic nerve repair comprises of a cylinder of around 15 mm length and 1.5 mm diameter (14) (Fig 2). Although this can be readily meshed using COMSOL, the discrete and continuous components of the model have different requirements: the continuous models require a dense lattice for convergence, the random walk is lattice-based and requires the spacing between mesh nodes to be approximately the growth rate of neurites (≈10 $\mu\mathrm{m}.\mathrm{h}^{-1}$ (γ)). The time step between iterations was fixed at 1 hour as it was found to be a good compromise between ensuring computational efficacy and space availability of nodes when simulating thousands of neurites.

A standard finite element mesh comprises tetrahedral or hexahedral elements, which for a mesh of a 15 mm length NRC with an inter-node separation of around 10 μm would make the model computationally prohibitive. Instead, a mesh was constructed for a circular cross-section at either the distal or proximal end of the NRC with a resolution representative of a neurite growth rate (e.g. inter-node separation around 10 μm) (Fig. 3 A) and then extrapolated down the length of the cylinder, using a COMSOL tool called “swept” (Fig.3 B) resulting in equally spaced nodes.

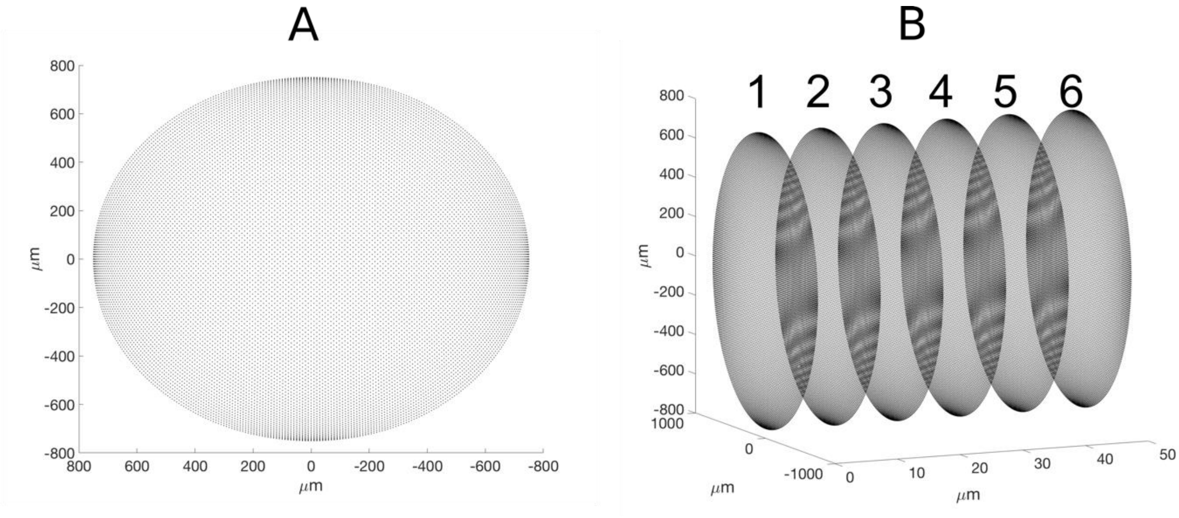

Fig 3: Meshing an NRC geometry.
First of all, a circular cross-section through the proximal end of the NRC cylinder is meshed ensuring the nodes are at a mean distance of 10 μm (A) and secondly the remaining geometry is meshed by 'sweeping' with a mean distance of 10 μm along the length of the NRC creating copies of (A) as exemplified by the 1 to 6 cross-sections (B).

We present a case study to demonstrate the computational model, where the radius (r) and number (n) of PGFs embedded in an NRC are optimised to maximise the regrowth of neurites. These PGFs are captured *in silico* by an algorithm that defines the nodes that the PGFs occupy, and excluding them from the available domain for neurite paths. The algorithm starts by considering the nodes at the proximal cross-section of the device (S), and randomly distributing PGFs, taking account of both their radius, and proximity to neighbouring fibres and the edges of the NRC. The distribution algorithm ends when either the desired number of PGFs have been included, or when there are not enough nodes available for more fibres to be included. The nodes in the proximal cross-section that correspond to PGFs and excluded from the neurite domain, are then extrapolated down the length of the NRC.

We assume that the PGFs provide a stiffness cue, which influences the growth rate of neurites that are close enough to be affected. This is achieved by associating a higher stiffness value to nodes within a fixed radius (α) of each PGF, and again extrapolating down the length of the NRC. The PGF distribution algorithm is summarised in the Algorithm 1.

Algorithm 1: placing the PGFs within the NRC

```
Initialise: the user decides on the number of fibres ($\boldsymbol{n}$) and the radius of the fibre ($\boldsymbol{r}$) and the thickness of the stiffer area surrounding the fibres ($\boldsymbol{\alpha}$).
Taking the nodes ($\boldsymbol{S}$) from the most proximal side.
Pre-process $\boldsymbol{S}$ so that it only includes nodes that are at a distances $\leq \boldsymbol{r}$ from the edge of the geometry.
while $\boldsymbol{i} < \boldsymbol{n}$
  A node $\boldsymbol{s_i} \in \boldsymbol{S}$ is chosen at random.
  All the nodes at a distance $\leq \boldsymbol{r}$ from $\boldsymbol{s_i}$ are found and removed from $\boldsymbol{S}$.
  Then nodes at $\boldsymbol{r} <$ distance $\leq \boldsymbol{r} + \boldsymbol{\alpha}$ are given a higher stiffness values to the remaining $\boldsymbol{k_\alpha}$ (see section 2.2.2).
  if there are no nodes left in $\boldsymbol{S}$
    break
end while
'Sweep' the nodes that belong to the fibres and the stiffness area along all the whole geometry of the NRC.
```

2.2 Computational Model of Neurite Growth

2.2.1. A General Framework for Neurite Growth

We develop a computational model for neurite growth using a random walk framework based on a simplified version of the Langevin equation, which describes the Brownian motion of particles, which is a common approach in the literature (17,18). For a cell tip at position $q(x, y, z, t)$ on a substratum at time t, the Langevin equation states that the movement of the cell can be described by:

$$m\frac{\partial^2 q}{\partial t^2} = -\zeta\frac{\partial q}{\partial t} + F(t), \tag{1}$$

where m is the mass of the cell and $\frac{\partial q}{\partial t}$ and $\frac{\partial^2 q}{\partial t^2}$ are the cell speed and acceleration, respectively. Equation (1) can be interpreted as Newton's second law of motion under the assumption that the cell experiences only two forces: (1) a drag force $-\zeta\frac{dq}{dt}$ with drag coefficient ζ that represents all the forces that impede cell tip movement and (2) stochastic motion described via $F(t)$. This description provides the components required to simulate cellular random motility such as stochasticity and persistence or inertia. It can be extended to account for directed motion by adding a term that defines, e.g. haptotaxis (19,20), chemotaxis (19,21,22) and galvanotaxis (23). Furthermore, a white noise term of the form $dB\big(t, k(q)\big)$ (where $k(q)$ is the stiffness of the extracellular matrix) can be included to capture the cell mechanisms responsible for stiffness sensing in the case of durotaxis (here q is a constant) (18).

The work by Zubler and Douglas (7) simplifies Eq. 1, assuming that the Reynolds number associated with neurite movement is small (in the order of 10^{-7} (24)),

$$\frac{dq}{dt} = \sum F(t). \tag{2}$$

Computationally, Eq. (2) can be approximated using the explicit Euler method, with the displacement of the cell tip (Δq) at each time step (Δt) given by:

$$\Delta q = \left(\sum F(t) \right) \Delta t. \tag{3}$$

As the model developed is lattice based, following Segev and Ben-Jacob (25) Eq. 3 is further simplified by assuming Δt is constant and in this particular case equal to 1 hour. In addition, the term $F(t)$, for a lattice based random walk, will be associated with the sum of cues present at a particular node ($w = 1 \dots M,$ where M is the total number of nodes in the mesh) in the mesh, hence, Eq. 3 is reduced to:

$$q_{t+1} = q_t + F(w). \tag{4}$$

The forces associated to each w are defined based on a formulation established by Segev and Ben-Jacob (25),

$$F(w) = M(\theta_w) + P_w(t), \tag{5}$$

where, $M(\theta_w)$represents the mechanical resistance of neurites to bending, and the term $P_w(t)$ is an aggregate representation of the environmental cues (represented by P_w when evaluated at node w) that the neurites respond to (e.g. chemotactic, durotactic). The term $P_w(t)$ is prescribed based on an individual scenario, as demonstrated in the case study section. Following, the work by Segev and Ben-Jacob, the term $M(\theta_w)$ is described through a probability density function (PDF) that associates a probability to the angle (θ_w) that successive neurite segments will make between each other (see Fig 4). In Segev and Ben-Jacob (25), $M(\theta_w)$ is defined ad-hoc, here it is informed by experimental data, as described through the case study.

To the authors knowledge, there are no direct experimental data to characterise the functions $M(\theta_w)$ and $P_w(t)$. To proceed, we normalized each relationship to minimise the required parameters to those representing the weighting of the different cues. To guarantee physiologically-realistic and smooth neurite paths, the mechanical resistance term is always weighted higher than all the other forces simulated.

After meshing the geometry, from the total number of nodes (U) in a surface, such as in Fig. 3 A the initial position (x) of N neurites is chosen following a normal random distribution $P(x)$ as:

$$P(x) = \begin{cases} \frac{1}{U}\ for\ x < U \\ \\ 0, otherwise \end{cases}, \tag{6}$$

At each subsequent time iteration, an array (L_N) is created that holds the nodes (m) that are at a distance of 10$\pm\delta$ μm from each neurite, where δ is a parameter chosen to mitigate any directional bias. The probability associated with moving to each subsequent node is calculated using Eq. 5. For each neurite and at each timepoint, a sum (C_N) is calculated of the probabilities of moving to each subsequent node ($w = 1 \ldots \vartheta$),

$$C_N = [F(1),\ F(1) + F(2),\ F(1) + F(2) + F(3),\ \ldots, F(1) + \cdots + F(\vartheta)], \tag{7}$$

where the largest value in the array C_N will be associated to the w_i with the largest F_w value. A random value (X), between 0 and $F(1) + \cdots + F(\vartheta)$, is then generated and the array T_N is calculated as:

$$T_N = C_N - X. \tag{8}$$

From T_N the index (γ) of the first positive value is found, and the node chosen for next time iteration of the algorithm is that associated with index (w_γ). The simulation ends after 8 weeks (equivalent to $\Delta t = 1$ hour). The movement of neurites within a mesh is illustrated in Fig. 4.

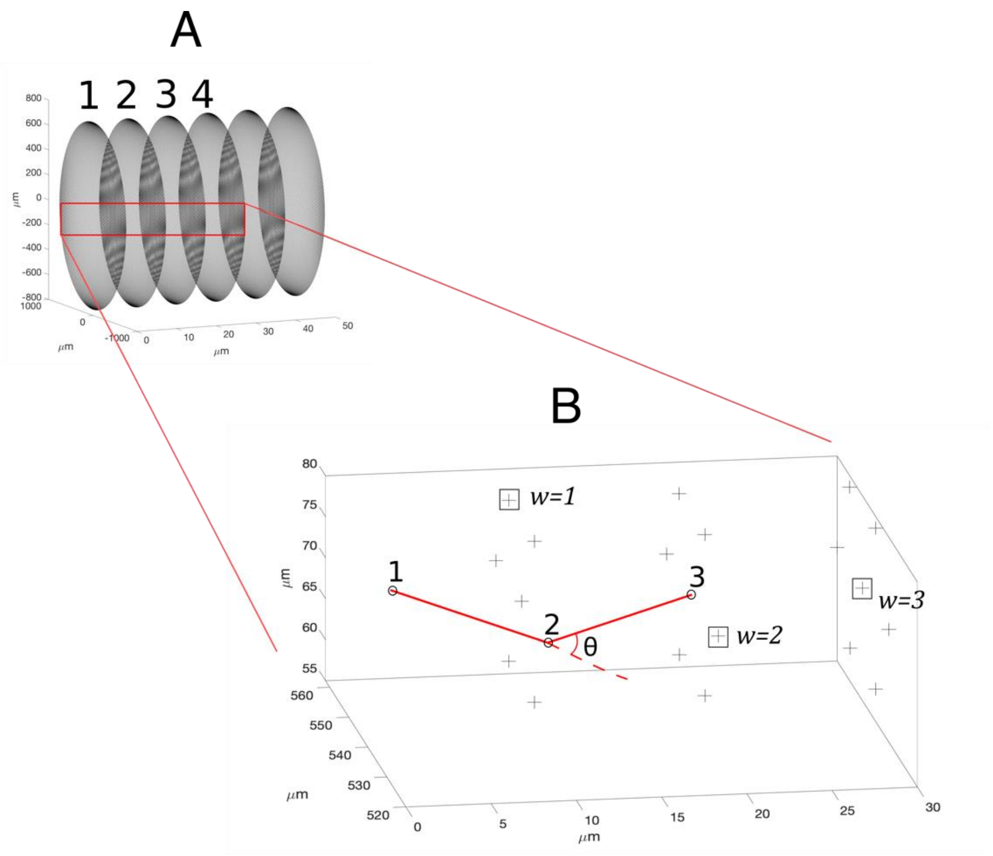

Fig. 4: Neurite movement inside a mesh.
A. The meshed NRC geometry, as described in Fig. 3 B, comprised of a meshed cross-section swept down the length of the NRC. Indicative cross-sections down the length are labelled 1,2,3,4. B. Schematic of a neurite tip starting at surface number 1, progressing to surface number 3 after 2 iterations. The neurite tip at surface 3 has the nodes (w) at surfaces 2, 3 and 4 to choose from for the next iteration, and the choice of this next position is informed by the PDF $M(\theta_w)$ (a function of the angle (θ) made between segments).

For simulations where the term $P_{w_i}(t)$ dominates the movement of neurites, the predicted neurite paths were not physiologically realistic due to sharp angles between neighbouring segments (Fig. 5 A). To mitigate this, and following the approach of Segev and Ben-Jacob (25), we introduce a noise reduction term that consists in finding a number (N_R) of arrays $T_{N_{i \dots N_R}}$ as

$$T_{N_{i \dots N_R}} = C_N - [X_1, X_2, X_3 \dots X_{N_R}]. \tag{9}$$

From each array a γ_i is identified as the first positive value for each array creating an array of indexes $[\gamma_1, \gamma_2, \gamma_3 \dots \gamma_{N_R}]$. Then a "winner takes all" methodology is implemented where the node selected the largest number of times is the node chosen for the next iteration. This methodology ensured the neurite paths were more physiologically realistic, as shown in the results section (Fig. 5 B).

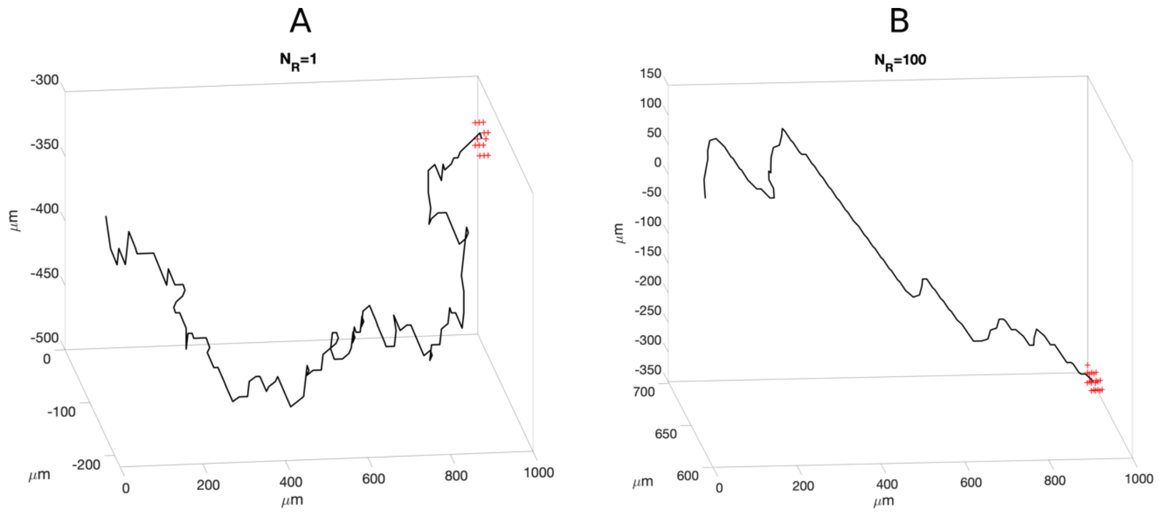

Fig. 5: Illustration of the need for the noise reduction parameter N_R.
A. $N_R = 1$ resulting in a neurite path that frequently includes straight angles, which is not physiological, B. $N_R = 100$ resulting in a much straighter path compared to A.

Two further conditions were implemented. First of all, to prevent neurites from crossing each other, all nodes that have been occupied by each neurite are excluded from the node array L_N. Secondly, the neurites paths are constrained by the boundary of the NRC, as they only have the nodes within the domain available to them.

It is also necessary to ensure that nearby neurites do not choose the same node at the next iteration. When a number of neurites (ε) share a node in their L_N, an array of cumulative probabilities is built, where all neurites have the same probability of being chosen ($\frac{1}{\varepsilon}, \frac{2}{\varepsilon}, \frac{3}{\varepsilon} \dots \frac{\varepsilon}{\varepsilon}$). A random variable is generated ($0 \leq X < 1$) and the same procedure as in Eq. 7 is followed to choose the neurite to which the node is apportioned, and the node is removed from the available paths of all other neurites.

This computational framework enables prediction of neurite paths, that incorporate competition for space. The framework is summarised through a pseudocode in Algorithm 2. Next we describe how to implement the framework for a specific scenario. All the code created can be found in the Supplementary material.

Algorithm 2: Computational Implementation of Neurite Growth Algorithm

```
12:     Initialise: user chooses the number of neurites simulated ($N$) and, assuming the
        starting time is ($t = 0$), the duration ($t_{end}$).
13: All $N$ neurites at t=0 are distributed randomly across the distal cross section of the NRC
14: while $t < t_{end}$ do
15:   Build the array $L_N$ of nodes ($m$) at a distance < 10$\pm\delta\mu$m.
16:   Remove all the nodes that are occupied by neurites as well as the ones belonging to
      matrix $\mathbf{O}$, which are outside the geometry of the NRC.
17:   if $\varepsilon$ neurites detected the same node do
18:       Generate random variable $X$ between 0 and 1 with each neurite having probability
          $\frac{1}{\varepsilon}$ of being chosen.
19:       The first neurite that has $[0, \frac{1}{\varepsilon}, \frac{2}{\varepsilon} \dots \frac{\varepsilon}{\varepsilon}] - X > 0$ is chosen.
20:   end if
21:   Calculate $\theta$ between neurite consecutive segments.
22:   Get the value of the cues at the nodes detected ($P_{w_i}(t)$.)
23:   Normalize both $M(\theta_{w_i})$ and $P_{w_i}(t)$ respectively and calculate $F(w_i) = M(\theta_w) + P_w(t)$.
24:   Create the cumulative array $C_N = [F(1),\ F(1) + F(2),\ F(1) + F(2) + F(3),$
      ... $F(w_1) + \cdots + F(\vartheta)]$,
25:   Generate random variables $0 \le X_N < \sum_{i=1}^{m} F(w)$
26:   Find the node at $\gamma$ which is the index of the first true value for $T_N = C_N - X > 0$.
27:   Perform step 14 and 15 $N_R$ times.
28:   The next position of the neurite is the node that has been most frequently chosen.
29:   $t = t + \tau$, where $\tau$ is the time step considered.
30: end while
```

2.2.2 Case Study: Phosphate Glass Fibres Embedded in a Cellular Hydrogel

The computational model is applied to a specific scenario to demonstrate its utility. We focus on an NRC with phosphate glass fibres (PGFs) embedded within an aligned cellular matrix, in order to provide additional directional and stiffness cues to neurites.

Engineered Neural Tissue (EngNT) comprises an aligned cellular collagen matrix. A typical *in vivo* test for EngNT is summarised in Georgiou *et al*. (12), where an EngNT construct is tested in a 13 mm nerve gap in a rat sciatic nerve injury model. After 8 weeks, the number of neurites is counted in 4 cross-sections through the construct, through histological staining and segmentation. These 4 cross-sections are measured from the end of the nerve stump, specifically, 1 mm into the proximal (PS) and distal (DS) stumps and 1 mm into the proximal (PD) and distal (DD) parts of the repair site (see Fig. 6).

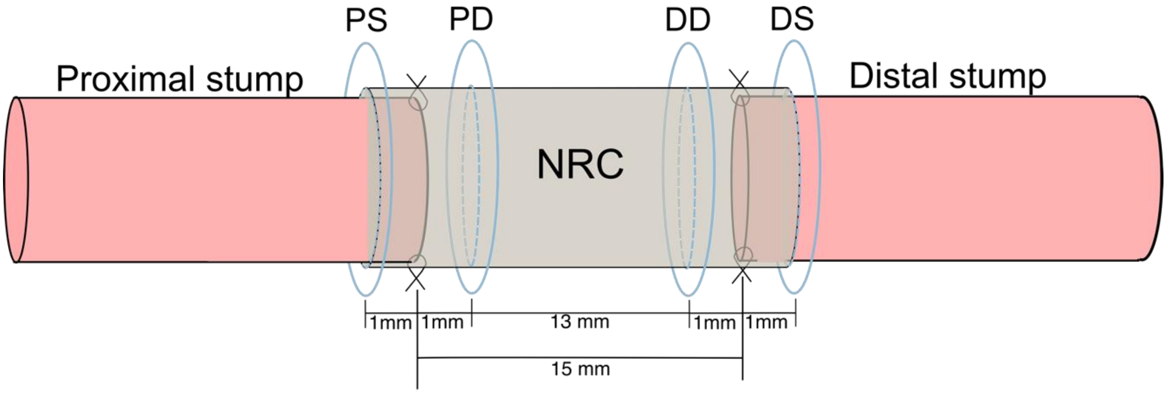

Fig. 6: Schematic diagram indicating the nerve repair and NRC geometry, and locations where neurite regeneration are assessed using histological staining. This represents a typical *in vivo* setup for assessing nerve injury repair in a rat sciatic nerve model. In the example scenario reported in Georgiou *et al*. (12), neurite numbers were counted in cross sections at 4 locations 1 mm into the proximal (PS) and distal (DS) stumps, or 1 mm into the proximal (PD) and distal (DD) parts of the repair construct, measured from the end of the nerve stump in each case. These data are used to inform the computational modelling framework.

Georgiou *et al*. (12) counted around 4,000 neurites at the PS, of which around 50% made it to the PD after 8 weeks; of these, 70% were recorded at the DD. For the control scenario of an empty tube (no aligned matrix filling), a similar number of neurites made it from the PS to the PD cross-section, but only 10% made it to the DD, as summarised in Table 1.

Table 1

Repair construct	**Neurite counts**			
	PS	**PD**	**DD**	**DS**
Empty tube	4,000	2,000	200	200
EngNT	5,000	2,000	1,400	1,000

Neurite counts extracted from Figure 4.18 of the work by Georgiou (26)

Here we explore the scenario where, following the approach in (15), PGFs are embedded in the EngNT scaffold, to provide an additional directional and stiffness cue to encourage more neurites to reach the DD within 8-weeks. First of all, we present the provision of parameter values and constitutive relationships in the computational model, using the prescription of the environmental cue term, $P_w(t)$. All parameter values are summarised in Table 2.

Table 2

Parameters	Definition	Value
γ	Growth rate of neurites.	10 μm.h^{-1}
δ	Standard deviation of growth rate.	0.7 μm.h^{-1}
n	Number of fibres embedded within the NRC.	To be determined via optimisation
r	Radius of each of the n fibres.	To be determined via optimisation
N	Number of neurites initiated at the PS.	2000-4000 taken from experimental (12)
β_μ	Constant that represents the forward directional bias $B(w)$ when a neurite grows within EngNT.	Fitted
β_V	Constant, such as β_μ, it accounts for the forward bias, however, here for the empty tube.	Fitted
α	Thickness of the high stiffness zone surrounding a PGF	Investigated through sensitivity analysis
k_α	The neurite bias to move forward when in the stiffer area surrounding the PGF's.	Investigated through sensitivity analysis
N_R	The noise reduction term. (Eq. 9)	Fitted

Summary of the parameters in the computational model. Parameter values are either known based on experimental studies, fitted by comparing model predictions against neurite count data at the sections identified in Figure 6, or investigated through a model sensitivity analysis. Finally, the number and radius of the PGFs are determined by optimising to maximise the number of neurites that reach the DS.

Based on these experimental protocols defined in Georgiou *et al*. (12), the duration of simulations (t_{end}), the number of neurites simulated (N) were fixed, alongside the dimensions on the geometry. Next we prescribe the function $M(\theta)$, which encapsulates the direction of neurite growth in the random walk model (equation (5)), based on data from Razetti *et al.* (6), which reconstructed neurite architectures in 3D based on histological staining of gamma neurons in a drosophila model. Razetti *et al.* (6) were then able to segment the architecture with nodes separated by 11 μm and calculate the angles made between segments (Fig. 7). Such data resolution has yet to be achieved in rat models (although the model can be readily recalibrated when required).

These data are used to inform the function $M(\theta)$ by, firstly, calculating the distribution of angles between neighbouring neurite segments, and then fitting different forms of PDF's to the distributions, as demonstrated in Fig. 7. Normal, Logarithmic and Kernel distributions were all tested, and it is clear that the Kernel distribution comprised of the sum of normal distributions with a bandwidth of, approximately, 3.58 best captures the properties of the distribution.

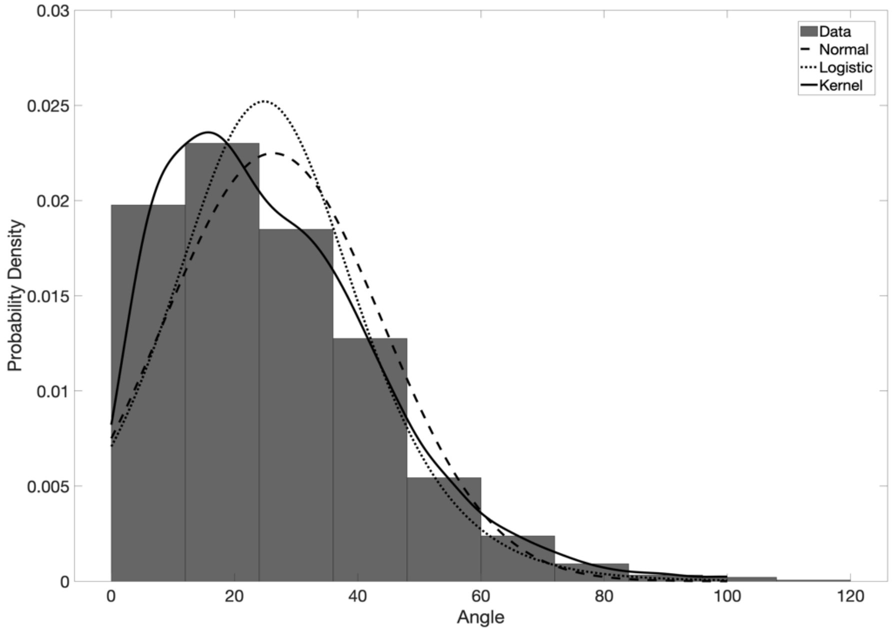

Fig. 7: Prescription of the PDF $\boldsymbol{M(\theta)}$ using data from Razetti *et al.* (6)
The function $M(\theta)$ from Equation (5) is calculated by fitting a PDF to angle distributions extracted from reconstructed gamma neurite architectures from a drosophila model by Razetti *et al.* (6). Different forms of PDF were tested, with the Kernel (bandwidth of 3.58) chosen.

The term $P_w(t)$ in the random walk model (Eq. 5) encompasses the role of environmental cues in determining the direction of neurite growth on the movement of neurites. Here, we consider the combined impact of environment cues provided by the EngNT (represented by the function $B(w)$, which includes both durotactic and chemotactic effects, and depends on the spatial location through w), and the durotactic cues provided by the fibres (represented by $D\big(\nabla k(w)\big)$, where $\nabla k(w)$ represents the stiffness gradient between the current neurite tip position and those at the following iteration locations, $k(w)$) so that

$$P_w(t) = B(w) + D\big(k(w)\big). \tag{10}$$

To the best of our knowledge, there are no clear data to inform these relationships directly in the literature. It was, then, assumed that the chemotactic and durotactic cues present in EngNT are represented as a constant bias of neurite tips moving towards the distal surface of the device ($\beta_\mu(w)$), similarly, a constant was defined to represent the cues in an empty tube ($\beta_V(w)$). These two constants were then fitted, as described in the following sections, to data consisting of neurite counts from Georgiou et al. (2013) for the empty and EngNT construct (and as summarised in Table 1). The parameter space is informed by ensuring that the forward bias $B(w)$ cannot be larger than the mechanical resistance $M(\theta_w)$, as it would result in nonphysiological behaviour, hence, as $M(\theta_w)$ has a value between 0 and 1; hence, as $M(\theta_w)$ we assume that $B(w)$ is between 0 and 1, with $M\left(\theta_{w_i}\right) \geq B(w)$.

Finally, the term $D(\nabla k_w)$ in equation (9) describes the response of neurites to the embedded PGF fibres. In (27), the modelling literature describing how cells respond to the stiffness of the extracellular matrix (ECM) is reviewed. These models focus on cell processes at different scales: at the subcellular scale, e.g. formation of focal adhesion the dynamics of protrusion and stress fibres (28–30), and at the cellular scale, where the main concern is the impact cells have on the structure of the ECM (31,32), or 2D cell motility via durotaxis (18). Our model follows a similar formulation to (25), with the term $D(\nabla k_w)$ depending on the difference between the stiffness value at the neurite tip at time t ($k(w_t)$) and sum of the stiffness values at all node options for the next time step (∇t) neurite tip location, $k(w_{t+\nabla t})$. In addition, an assumption is made that neurite tips only respond to increases in durotaxis and ignore decreases. In summary,

$$D\big(k(w)\big) = \begin{cases} k(w_{t+\nabla t}) - k(w_t),\ if\ k(w_t) \leq k(w_{t+\nabla t}) \\ 0,\ otherwise \end{cases}, \qquad (11)$$

The model is informed by a description of the stiffness field induced by PGFs. As summarised by the schematic in Fig. 8, we assume a zone of depth α, estimated to be approximately 20 μm from experimental observations, here the directional bias cells experience when in this stiffer area is modulated by a factor k_α. Furthermore, when the neurites are within the distance α from a fibre, their growth rate increases by a factor of two; the implementation of this is explained in later sections. All the effects of a PGF on neurite growth are summarised in Fig. 8.

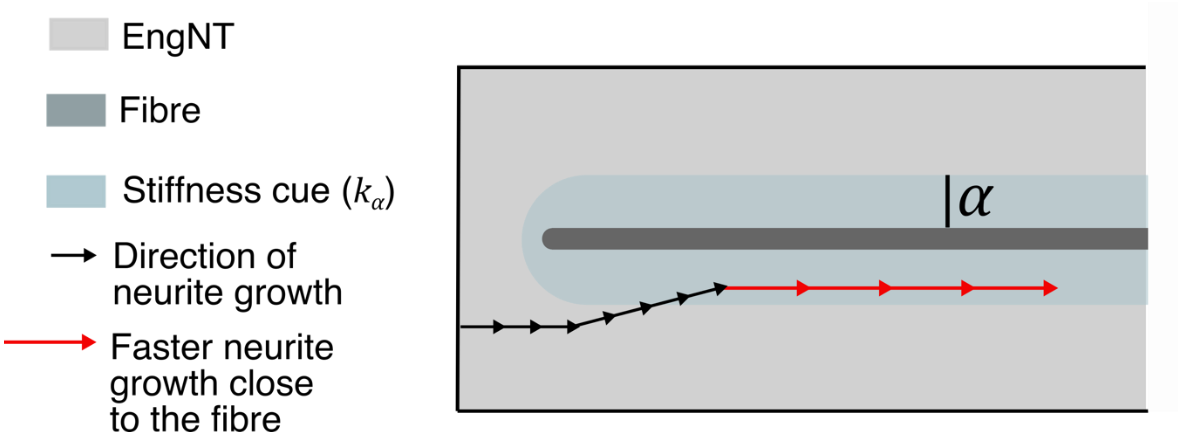
EngNT
Fibre
Stiffness cue (k_α)
Direction of neurite growth
Faster neurite growth close to the fibre
α

Fig 8: Summary of the impact of a PGF on the growth rate and direction of neurites. The PGFs are embedded throughout the EngNT within the NRC. In a region of depth α around a PGF fibre (depicted in light blue), the stiffness the neurite detects increases compared to the surrounding cellular matrix. Besides providing a directional bias, the region surrounding a fibre also induces a faster growth rate (by a factor of 2).

Parameterisation and Sensitivity Analyses: We parameterise the model by comparing its predictions against the neurite count data summarised in Table 1. Specifically, the parameters β_μ, β_V and N_R are informed through this process. The parameters β_μ and β_V define both the effect of cues (chemotactic, durotactic, etc.) on the neurite growth direction in an empty tube, as well as the increase in these cues when neurites move within EngNT. Hence, these two parameters are simultaneously optimised for both the empty tube scenario ($B(w) = \beta_V$) and when in the presence of EngNT ($B(w) = \beta_\mu$). The boundaries for the parameter space are summarised in Table 3. For all the fitting simulations the growth rate and standard deviation was kept constant (γ =10 μm.h^{-1} and δ =0.7 μm.h^{-1}).

Table 3

Parameters	Parameter space	Reasoning
β_μ	0 - 1	Chosen to ensure $M(\theta_{w_i}) \geq B(w)$ (Eq. 10).
β_V	0 - 1	Chosen to ensure $M(\theta_{w_i}) \geq B(w)$ (Eq. 10).
N_R	1 - 100	Defined ad-hoc.

Parameter space defined for fitting, which is done by comparing model predictions against experimentally measured data on neurite counts at different locations along an NRC.

The parameter space is large (several orders of magnitude), hence, a global optimisation such as the particle swarm optimisation (PSO) algorithm (33) was implemented. It consists in placing a number of particles (V) distributed throughout the parameter space. At each of their locations, they evaluate the function being studied and then each particle estimates the move it is going to make by comparing its previous positions to the best (closer to the optimal value) location, which is perturbed by a stochastic term. The next iteration is started after all particles have moved and progressively it is likely that all the particles move closer to the optimum value desired.

Two parameters need to be defined in order to implement the PSO, which include the number of particles (V) and the maximum number of iterations (G). These need to be chosen to ensure the model converges to the right solution. Here, V was defined as 30 and G was chosen in the order of hundreds of iterations.

The error minimized by the PSO algorithm was defined as the error between the experimental neurite count measurements, and the equivalent computational simulations. This error metric is calculated for both the empty tube scenario (E_H) and the EngNT embedded NRC (E_E) simultaneously, and perform the parameterisation by minimising the overall error function (E_T), defined as the mean between E_H and E_E.

Due to the computational costs of the PSO algorithm, trends of the PSO simulations over the first tens of simulations only were investigated. Through this process it was identified that the parameter β_μ always tended to the value of 1 and, therefore, it was omitted from further analysis and instead we focused on the remaining two parameters (β_V and N_R).

After optimising we quantified the dependency of the model predictions in the fitted parameter values, using the PAWN sensitivity analysis method devised by Pianosi and Wagener (34). There are several alternatives to the PAWN, the most commonly used being the Morris method (35); however, the Morris method requires many iterations to achieve convergence (36). In contrast, the PAWN method is not a moment-based method and instead uses the cumulative density function (CDF) of the models output (y), which for the model would consist in the percentage of neurites that make across the device, in response to input parameter values ($\boldsymbol{x}$, $\boldsymbol{x} = |x_1, x_2, x_3, \dots x_M|$) sampled at random from a user defined range, in order to devise a quantitative measure (PAWN) to apportion the uncertainty of the output to each parameter.

The method consists in creating, an unconditional CDF ($F_y(y)$), where all the parameters are varied at random within the ranges established for a number of samples (J_U). For each parameter, a number of values (j_C) are chosen and n_C different CDFs ($F_{y|x_i}(y)$) are constructed for each parameter in turn; for each CDF a parameter value is chosen and is maintained constant, whilst the remaining parameters are varied randomly over a number of samples (J_C). The PAWN measure consists in the Kolmogorov-Smirnov (KS) statistic between the F_y and each $F_{y|x_i}$ for each parameter, calculated as:

$$KS(x) = \max_{y} \left| F_y(y) - F_{y|x_i}(y) \right| \tag{11}$$

The parameters that have the largest KS are the ones that have a more determinant impact on the model outputs.

This method is employed to test the sensitivity of the predictions of the model to the parameters: the growth parameter in Eq. 10 (β_V), the noise reduction (N_R) in Eq. 9, stiffness parameter (k_α) in Eq. 11, the depth of the high-stiffness zone surrounding PGFs (α) (Algorithm 1), and the standard deviation of the growth rate (δ) (Algorithm 2). The parameter ranges chosen are summarised in Table 4. Throughout, J_U, J_C and j_C are fixed at 100, 100 and 5 respectfully.

Table 4

Parameter	Range
$\boldsymbol{\beta_V}$	$\pm 20\%$ of the value fitted
$\boldsymbol{N_R}$	$\pm 20\%$ of the value fitted
$\boldsymbol{k_\alpha}$	1-3 [dimensionless]
$\boldsymbol{\alpha}$	10-80 μm
$\boldsymbol{\delta}$	$\pm 20\%$ of the value identified in Table 2

Ranges used to perform the PAWN analysis.

Optimization: The aim of this work is to identify the optimal radius (r) and number (n) of fibres embedded within the device to ensure the largest number of neurites cross the full length of the device. Increasing the number of PGFs increases the total cues that promote growth towards the distal stump; however, PGFs also take up space which may become limiting, and therefore optima may be identified. The impact of different numbers of fibres on the behaviour of the neurites in a 100 μm length NRC is illustrated in Fig. 9, with 5 (Fig. 9 A,B,C) or 100 (Fig. 9 D,E,F) embedded PGFs after 0, 5 and 10 hours of simulation. The number of neurites that reach the distal stump is approximately 1-3% versus 80% for 5 versus 100 PGFs, respectively.

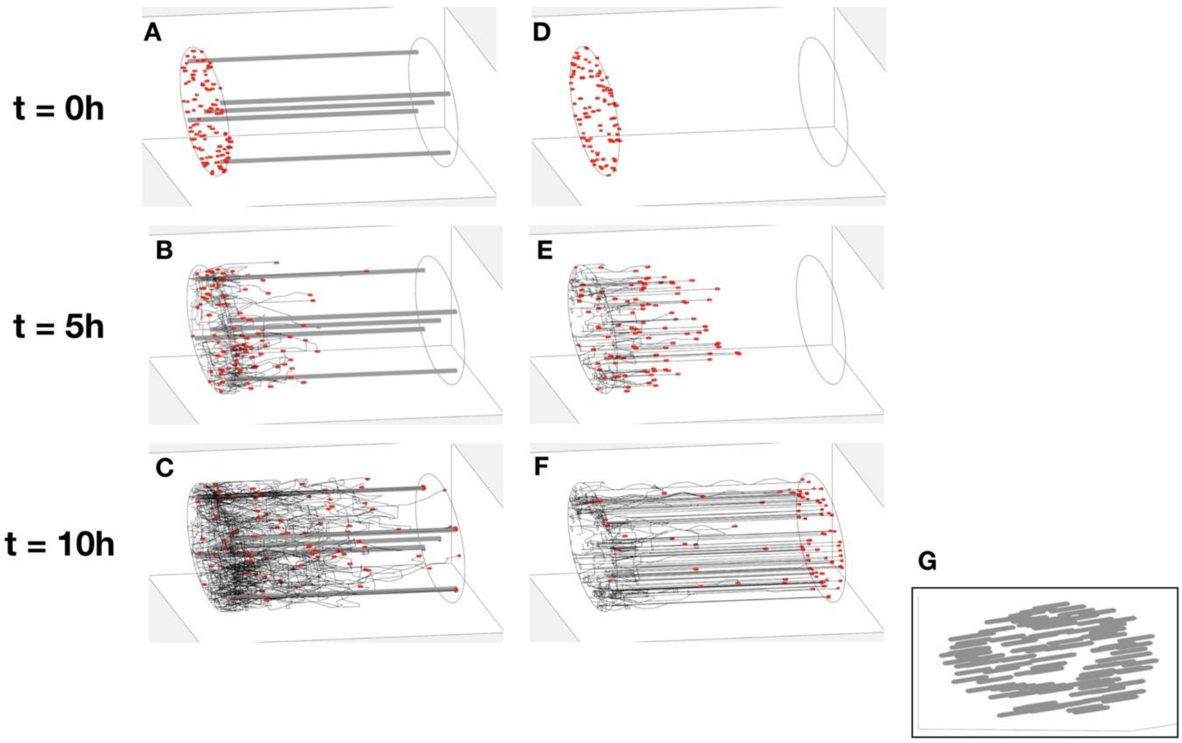

Fig. 9: Indicative Simulations of Neurite Growth.
Simulations of neurite growth in the presence of 5 (top) versus 100 (bottom) PGFs, with simulation outputs demonstrated at 0 h (A, D), 5 h (B, E) and 10 h (C,F). Red dots indicate the neurite tip. For the case of 100 fibres the fibre distribution through the proximal stump cross-section was plotted separately (G) in order to allow for visualisation of neurites. Videos of these simulations can be found in the Supplementary Material.

A PSO algorithm is utilized again, with parameter ranges for the PGF radius and number prescribed. The minimum PGF radius was based on feasibility of manufacture (15 μm (37)), and the maximum was set to be the radius of NRC (750 μm). The number of fibres is limited by the number of nodes present in the proximal surface of the mesh (approx. 14,000). For each particle of the PSO algorithm, a value for the two parameters is taken from the ranges described and the growth of 2000 neurites is simulated for 8 weeks.

The error function is dependent on the percentage of neurites that reach the distal stump (against a target of 100%). The PSO was terminated when the improvement between iterations was less than 1%.

Implementation: The model was developed using the LiveLink package provided by COMSOL to export its mesh building functionalities into Matlab and use it to build the require geometries. All the code was written in Matlab, including the PGF placement algorithm (§2.1), the neurite growth model (§2.2.1) and the PSO algorithm. For the latter, the implementation available in the optimization toolbox from Matlab (33) was used. The PAWN sensitivity analysis algorithm, was implemented following examples provided by the work of Pianosis *et al*. (36).

3. Results

Following the structure of the Methods section, we split the Results into three sections: the fitting of model parameters based on the experimental data presented in Table 1. (§3.1), the optimisation results for the PGF numbers and radius (§3.2), and the sensitivity analysis results (§3.3).

3.1 Fitting parameters to data

The forward bias parameters (β_μ and β_V) and the noise reduction term N_r were fitted to the neurite counts provided by Georgiou et al.(2013) (Table 1). For the parameter β_μ after hundreds of iterations of the PSO the 30 particles fitted the parameter to 1 with no variability. Hence, for the remaining analysis the parameter is going to be neglected and the focus will be on the β_V and N_r parameters. For these two parameters the range of parameters identified by the 30 particles is presented as box plots, as seen in Fig. 10. From both Fig 10 A and B it can be seen that all the particles converge to a set of values that varies by less than 1%.

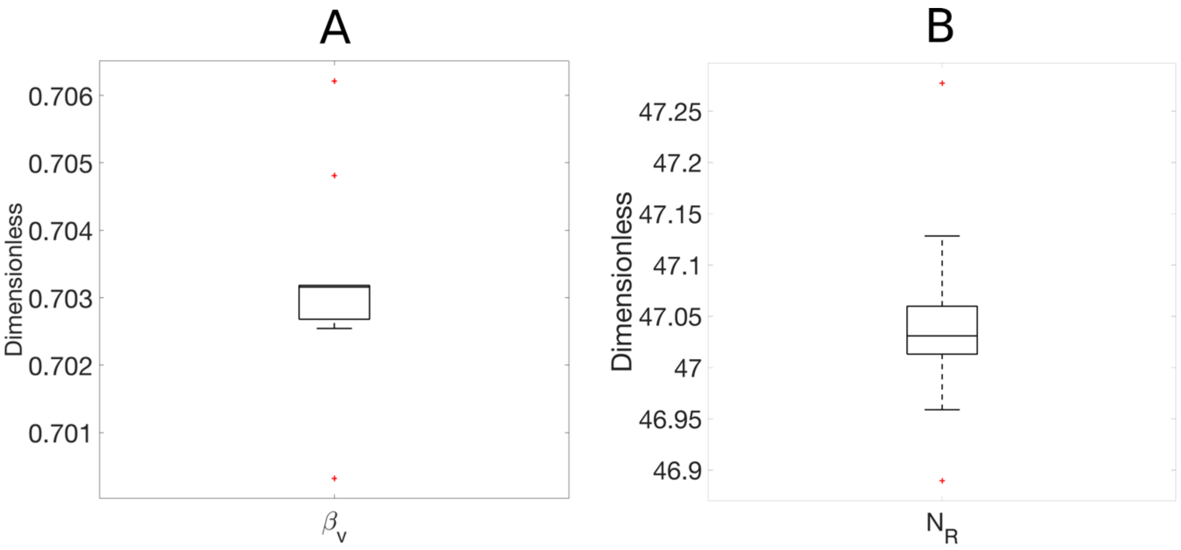

Fig. 10: The result of performing a PSO algorithm to fit the parameters β_V and N_R to the neurite counts for an empty tube and EngNT-filled NRC with no PGFs, based on experimental data on neurite counts summarised in Table 1 (from Georgiou *et al*. (12)).
Box plot of the result of the fitted parameters over 30 PSO particles, where the central line is the median, the box encompasses the interquartile range (25th to 75th percentile), the whiskers captures the whole data set and the red crosses present the outliers, for: (A) the β_V , that equates the bias of neurites of moving towards the distal side of the device and (B) N_R, the noise reduction parameter.

The robustness of the fit is dependent on the parameter variability, as shown in Fig. 11, which displays a box plot of the outcome of the 30 particles in terms of the error of the fitting for the individual EngNT embedded (A) and the empty devices (B). From the fits it can be seen that, within the quartile range, all the particles converged to values at maximum of 1% error from the required experimental values.

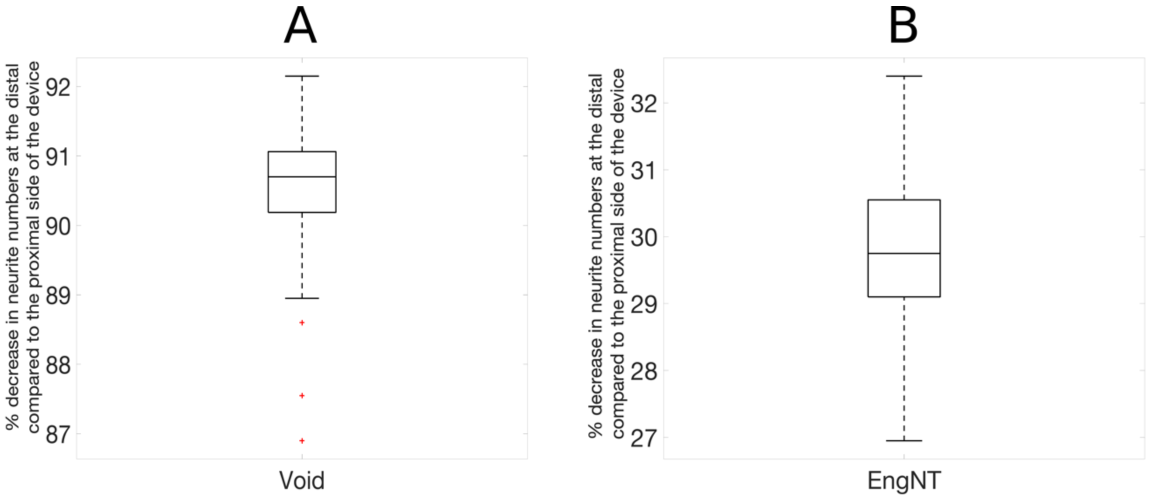

Fig. 11: Results from the PSO algorithm implementation to fit the model parameters to the data by Georgiou et al. (12) over 30 particles.
Box plot with central line representing the median and the box captures the interquartile range (25th to 75th percentile), the whiskers extend to encompass the data set except the outliers, which are presented as the red crosses for: (A) the error when an empty construct is simulated and (B) similarly the mean error is plotted for the simulations of an EngNT embedded device.

From the range of parameters found by the 30 particles it was assumed that for the following optimization the values of these parameters would be the mean of the particle population, as seen in Table 5.

Table 5

Parameter	Fitted value
$\boldsymbol{\beta_\mu}$	1
$\boldsymbol{\beta_V}$	0.703
$\boldsymbol{N_r}$	47.032

The fitted parameter values.

3.2 Optimization

Here the PSO algorithm was run until all the particles converged to a solution where more than 90% of neurites reached the distal stump within 8 weeks simulation timespan and the output of the optimisation is compiled over 30 particles. After hundreds of simulations of the PSO all particles converged to a radius of 15 μm, the smallest considered, with no variability between them. The optimal solution found consists in packing between 500 to 700 fibres with 15 μm radius within EngNT, resulting in 91% to 95% of neurites reaching the distal stump within 8 weeks (Fig. 12).

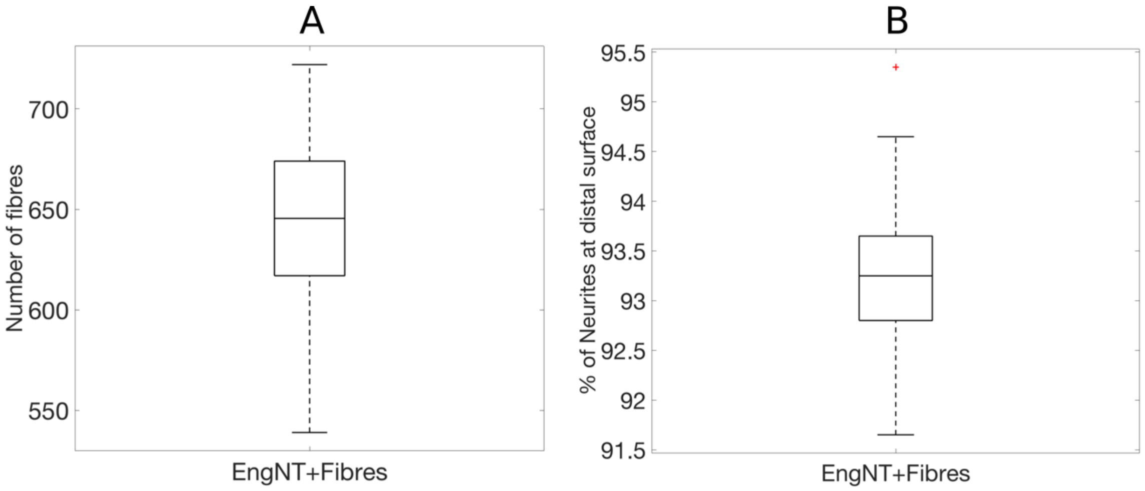

Fig. 12: Outcome of the PSO of the radius and number of fibres, with the variability over 30 particle runs demonstrated
Box plot representing the median and interquartile range (25th to 75th percentile), the whiskers encompass the whole data set, with the outliers represented by red crosses for: (A) the number of fibres embedded in an EngNT device and (B) the percentage of neurites that make it to distal side of the device.

The PSO algorithm demonstrated that the radious of the fibres should be15 μm the smallest manufacturable possible. A comparison of an empty tube or EngNT-filled NRC, for an increasing number of 15 μm-radius fibres is shown in Fig. 13.

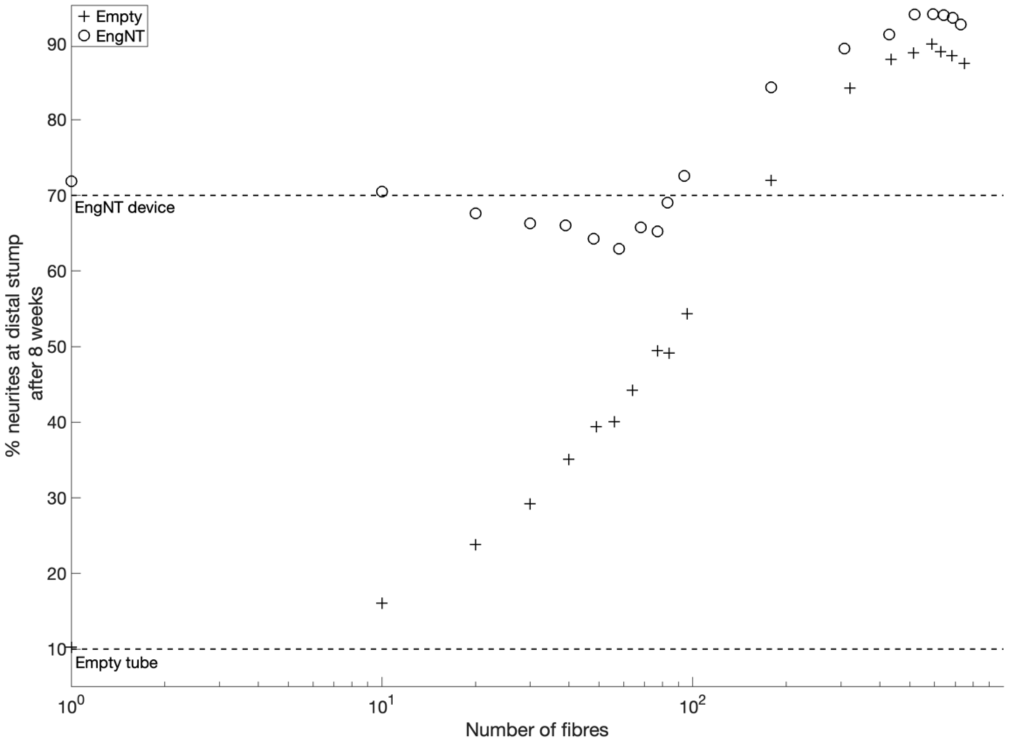

Fig. 13: Evaluating how varying the number of 15 μm radius PGFs for an empty tube and EngNT-filled NRC.
Simulations were performed for both conditions by increasing the number of PGFs from 1 to 900. Additionally, the experimentally measured values for those two conditions without PGFs are plotted as dotted lines.

3.3 Sensitivity analysis

The PAWN method was implemented to quantify the impact of changing parameters as described in Table 4 on the optimal predictions of model (around 650 fibres with a radius of 15 μm, resulting in 93% of neurites reaching the distal stump in 8 weeks). For each n_c value a CDF is constructed and Eq. 11 is used to identify each KS value, as presented in Fig. 14.

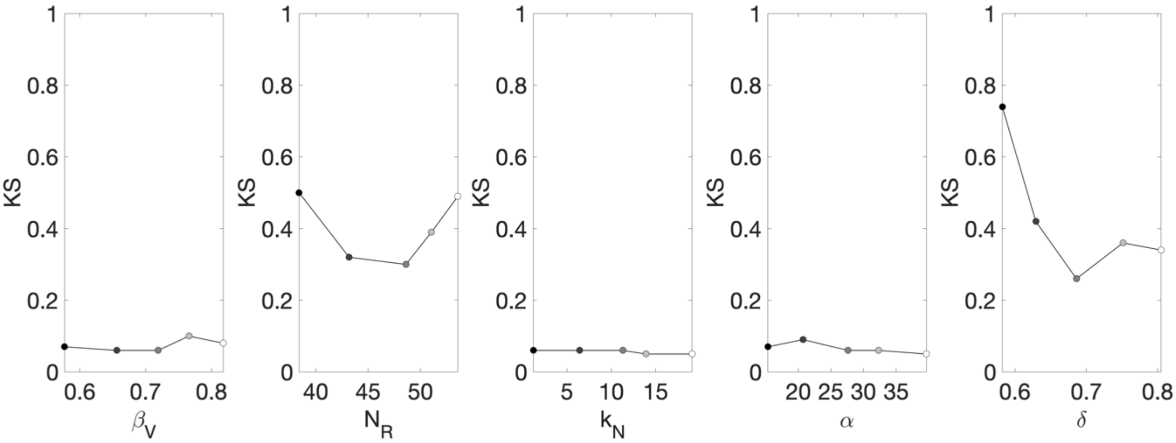

Fig 14: Summary of the Kolmogorov-Smirnov statistic measurements made for each parameter evaluated.
Each dot represents the maximum distance between one conditional CDF $((F_{y|x_i}(y))$, where the parameter being considered is kept constant and the remaining are varied at random, with the unconditional CDF $((F_y(y))$ following Eq. 11.

For each parameter, in Fig. 14, 500 simulations of the model are made. All simulations used to produce the unconditional CDF (F_y) were compiled into a box plot (Fig. 15), to observe how the number of neurites that make to distal side of the device in 8 weeks varies within the parameter space defined by Table 4.

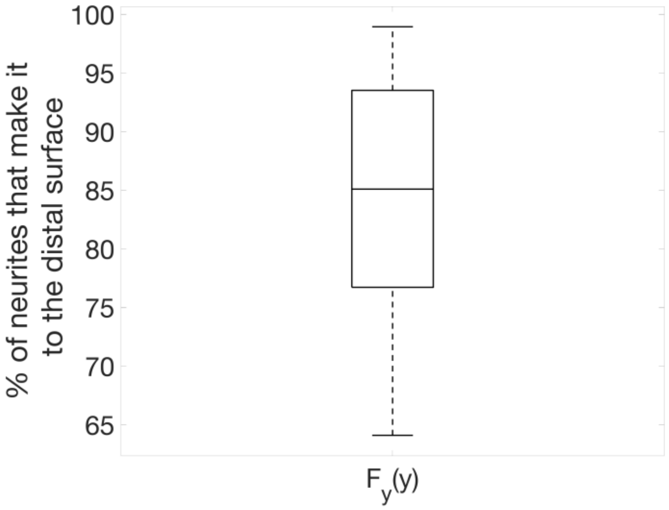

Fig 15: Variability of number of neurites that make to the distal side of the NRC, when parameters are varied, within the ranges presented in Table 4 following the PAWN method.
A box plot of all the model outputs when creating the unconditional CDF ($F_y(y)$) where with the median and quartile range (25th to 75th percentile) represented by the box and the whiskers capturing the whole data set except for the outliers, which are plotted as red crossed, where the line.

4. Discussion

The framework developed is applied to a specific case of the use of fibres as a method to promote the growth of neurites across the device. The predictions made are dependent on a series of factors, starting with the values of the parameters of the model, which is tested using the PAWN method. In addition, the model predictions are tested when the number of neurites is increased. All these subjects are further explored in the following sections.

4.1 Framework

The work developed follows similar principles as models in the literature (7,38), e.g. simulating neurites in 3D as latch dependent random walks, which results in the number of locations available to neurites becoming limited. Additionally, the latch is commonly built from hexahydral elements, which provides a larger degree of freedom.

Here a hexahydral mesh was not feasable because of the scale considered: thousands of neurites are simulated in a millimeter scale environment over weeks vs the models found, where tens to hundreds of neurites are considered within micron scale environment for hundreds of iterations. The architecture of the mesh can explain the fact that neurites get stuck around the fibres. The model by Razetti *et al.* (38), also, observed that their simulated neurites ran out of space to move.

Using, a PSO algorythm the parameter space can be optimally sampled arriving at a converging solution. The data available comprises of neurite counts and the cues provided by the devices considered are multi-faceted. Therefore, a qualitative approach was employed and as demonstrated it was possible to match the model predictions to data. However, the efficacy of the parameterisation reached is sensitive to small changes in parameter (Fig. 10-11), as a variability smaller than 0.5% results in the number of neurites crossing both device designs varying by, approximately, 3%. In order to address this it is recommended that a future *in vivo* experiment should quantify the number of neurites at several positions within the devices and over several time points.

Another set of data, taken from Razetti *et al.* (38), was used to parameterise the step size movement of neurites, which consisted in measurements from a different type of neurite. These data were required because of the difference in granularity of scale between the *in vivo* experiments and the *in silico* simulations. The data from Razetti *et al.* (38), as it described neurite movements between 10 μm segments. The two sets of data used were aquired from different conditions, different spicies and different types of neurons. Regardless, this work demonstrates a workflow that allows parametirisation of a neurite model by different sets of data and as relevant data are aquired the model can, easily, be adapted.

In addition, neurite counts from transverse sections do not allow an understanding of the impact of branching on the growth of neurites within these constructs, which is a known mechanism that neurites employ, in order to optimally sample their environment. However, its triggering mechanisms have not yet been properly characterised, therefore, models resort to making ad-hoc assumptions (7,38). Hence, as there are no data to properly parameterise a branching model, branching was not included. Without branching, which tends to be associated with temporary additional sprouts rather than increased functional neurite connections, the predictions of the model may overestimate the efficacy of the approaches under investigation.

4.2 Optimal therapy

A PSO algorithm was implemented to optimise the number and radius of the fibres embedded within a device, in particular, an EngNT filled device. From this analysis it was found that between 500 and 700 fibres with 15 μm radius should be embeeded in EngNT, resulting in a maximum efficacy of 94%.

This result is clearly demonstrated when neurites are simulated for an increasing number of fibres for both empty and EngNT devices, as seen in Fig. 13. In both cases the optimal number of 15 μm fibres was the same. Above 700 fibres the number of neurites that make it to the distal surface of device start dipping, which is because the fibres start to occupy larger amount of space. There are no simulations with a number of fibres above 900 because the fibre packing algorithm runs out of space to place them.

When observing the trends of the simulations it can be seen that, for the empty device, embedding fibres never results in less than 10% efficacy, as seen experimentally, for an empty constructs. At, approximately, 100-200 fibres the therapeutically efficacy of the therapy goes beyond the levels associated experimentally with EngNT alone, and a maximum is reached of 90%, when between 500 to 600 fibres are embedded.

When considering the EngNT it can be seen that, the number of neurites decreases down to, approximately, 60%. This is due to the distribution of stiffness cues being concentrated, resulting in neurites congregating around the existing fibres and running out of locations to move to and getting stuck, illustrating that the spatial distribution of these cues are crucial for the success of the therapy. Additionally, as aforementioned this is due to the fact that *in silico* the neurites are moving in a discretised and limited space. Moreover, as previously stated, this effect is common to other mathematical models.

When the number of fibres embedded in EngNT goes above 100 this provides the cues required to increase the number of neurites that make it to the distal end of the device, reaching a number approximately the same as the one achieved through the PSO algorithm of 94%. This result now needs to be tested experimentally.

Regardless of the of the number of neurites that cross the device, all simulations point to the fact that fibres should be as thin as possible. Going down to the minimum radius allowed to be simulated within the framework, of 1 μm, simulations similar to the ones presented in Fig. 13 were performed and it was found that the placing of 1 μm fibres within any of the devices resulted in an improvement above their individual fibre-free plateaus, reaching a maximum above 95% between 1,000 to 2,000 and decreasing to approximately zero when the number of fibres approaches 10,000. The optimal value is understandable since there is a ratio of almost one fibre per neurite, hence the majority of neurites can experience an increase in growth rate, without running out of space, due to the fibres. However, all our predictions assume that the radius of the cue surrounding each fibre is kept constant, which has yet to be validated experimentaly.The simulations discussed can be seen in Fig. 16.

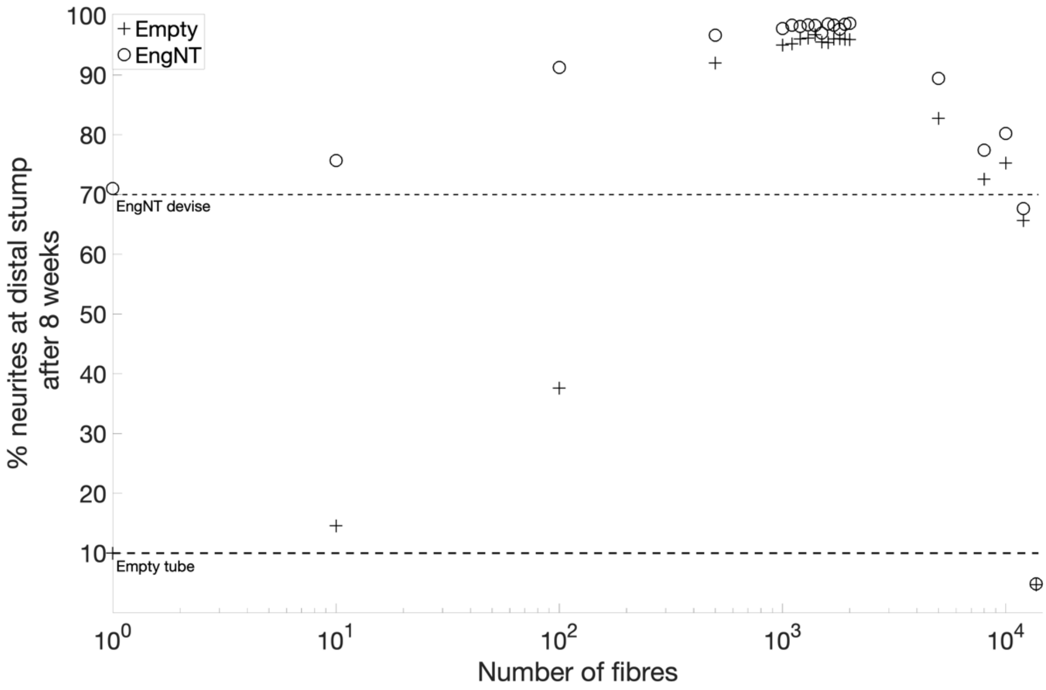

Fig. 16: To quantify the effects of reducing the radius of fibres to 1 μm on the predictions of the model, as in to Fig. 13, the model was simulated with an increasing number of fibres from 1 to 11,000.
As before two sets of simulations were performed to account for the NRC designs considered; fibres embedded within the EngNT and the empty device.

In summary, it is now required to investigate the translation of these predictions using *in vitro* and *in vivo* models. These studies can follow the protocols already developed by Georgiou et al. (2013) and Kim et al. (2015), however, the *in vitro* models need to mimic the spatial constraints of thousands of neurites growing and competing for space.

4.3 Robustness of predictions

In order to understand the dependency of the predictions of the model on the model parameter values, the PAWN methodology (34) was chosen due to the fact that it is not moment dependent and it produces graphical outputs of hierarchy of the parameters. However, Puy *et al.* (36) has shown that the outputs of the PAWN are dependent on how it is parameterised. The limitations of this method can be easily observed when looking at Fig. 14 where the KS values are evaluated at 5 points for each parameter at random leaving the parameter space between those 5 points unsampled, which, as this is a nonlinear model, might result in indeterminant behaviour.

Regardless, this method aims at presenting a hierarchy of the importance of parameter values on the predictions of the model (Fig. 14) and the outcomes of this analysis are consistent throughout the KS values. The parameters β_v (forward bias), α and k_α (stiffness cues surrounding the fibres). The smaller impact of the latter parameters is explained, as the distribution of stiffness cues is maintained within the parameter ranges chosen. The negligible impact of forward bias on the model is explained by the fact that it is modulated by the noise reduction term N_R, hence, although β_v makes the probability of moving forward larger than going in any other direction, it does not get chosen if the noise reduction does not allow it. Additionally, it is explained by the assumption made that the term $B(w)$ cannot have a higher probability than the $M(\theta)$. The sensitivity to N_R is clear in Fig. 14 as the KS value increases, when the parameter increases and decreases below the fitted value by 20%. Even when the parameter is varied by 10% the impact on the model output is larger than most parameters except δ.

The importance of N_R underlines the need to uncover the cellular mechanisms responsible for cell motility in response to durotactic cues. Here a simplified model was implemented to ensure the model is manageable, however, when developments are made in this field, the framework presented can easily be adapted.

The PAWN method identified growth rate standard deviation (δ) as the most impactful parameter (Fig. 14), which will impact the outputs of the model in two ways: 1. neurites will move for a smaller distance for each iteration and 2. the neurites have less space to move in the case that they share nodes. Alternatively, when increasing α the impacts on the model inputs are not so severe, which is explained, in part by the range of values chosen for α and the fact that the spacing between nodes is the same. In summary, when the quantitative measure to evaluate the importance of the different parameters on the predictions of the model is the distance travelled by the neurites, then it is rational that the choice of growth rate will lead to drastic changes in that measure. However, the model does handle neurites with different growth rates, as long as they are integer multiples of each other.

The PAWN method allows the robustness of the model predictions to be analysed. As seen from the unconditional CDF ($F_y(y)$) in Fig. 15, the majority of the simulations (65%) predict that approximately 600 fibres with 15 μm radius will improve the regenerative potential of an EngNT device by 1% to 20%. Therefore, there is a clear need to validate this result experimentally.

To investigate the importance of the number of neurites simulated on the predictions of the model, simulations were performed, where the number of neurite is increased to those counted at the PS crossection (4,000) in Table 1 (Fig. 12). This requires re-parameterisation of model, which can be found in Supplementary material.

Neurite growth in response to an increasing number of fibres embedded was, again simulated (Fig. 17) and a similar trend as in Fig. 13 was observed. The most crucial output is that the maximum achieved, when 500 to 900 fibres are embedded, is, approximately, of 71%. Compared to the maximum in Fig. 13, when considering fibres of 15 μm radius, both there is a decrease of 20%, which illustrates the limits of the predictive power of the model as with 4 thousand neurites and hundreds of fibres the number of nodes in the mesh available for neurites to move to is reduced substantially.

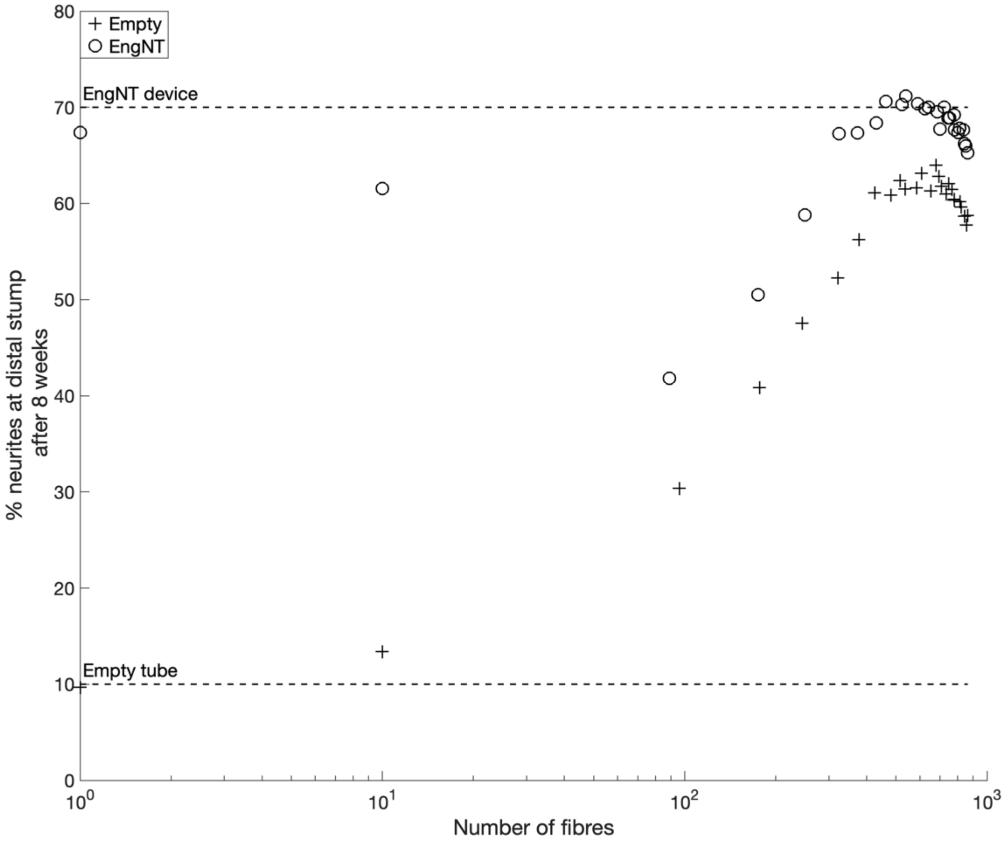

Fig. 17: Testing increasing the number of neurites.

Again, the behaviour of the model is evaluated for an increasing number of 15 μm fibres, however, here the number of neurites is increased by 100%.

Regardless, these results demonstrate that the potential of using fibres as a therapeutic tool for nerve repair is strictly dependent on the number of neurites the device hopes to accommodate. When aiming to guide the number of neurites that are reported to enter the device, embedding fibres in EngNT appears to be a valuable strategy, conversely, when targeting the neurites counted at the PS surface the potential of the therapy closely matches the efficacy of embedding EngNT alone in the device. Hence, the device needs to be modulated to address an exact therapeutic aim, in order to avoid underwhelming results. In addition, when designing *in vitro* models to test different iterations of the device the spatial dynamics of an *in vivo* case need to be replicated. The common neglect of this consideration might explain the difficulty in translating *in vitro* observations to *in vivo* models.

5. References:

1. Chen S, Chen Z-G, Dai H, Ding J, Guo J, Han N, et al. Repair, protection and regeneration of peripheral nerve injury. Neural Regeneration Research. 2015;10(11):1777.

2. Ruijs AC, Jaquet J-B, Kalmijn S, Giele H, Hovius SE. Median and ulnar nerve injuries: a meta-analysis of predictors of motor and sensory recovery after modern microsurgical nerve repair. Plastic and reconstructive surgery. 2005;116(2):484–94.

3. Scheib J, Höke A. Advances in peripheral nerve regeneration. Nature Reviews Neurology. 2013;9(12):668.

4. Pedrosa SS, Caseiro AR, Santos JD, Maurício AC. Scaffolds for peripheral nerve regeneration, the importance of in vitro and in vivo studies for the development of cell-based therapies and biomaterials: state of the art. Scaffolds in Tissue EngineeringMaterials, Technologies and Clinical Applications. 2017;9(12):179.

5. Angius D, Wang H, Spinner RJ, Gutierrez-Cotto Y, Yaszemski MJ, Windebank AJ. A systematic review of animal models used to study nerve regeneration in tissue-engineered scaffolds. Biomaterials. 2012 Nov;33(32):8034–9.

6. Razetti A, Descombes X, Medioni C, Besse F. A Stochastic Framework for Neuronal Morphological Comparison: Application to the Study of imp Knockdown Effects in Drosophila Gamma Neurons. In: International Joint Conference on Biomedical Engineering Systems and Technologies. Springer; 2016. p. 145–66.

7. Zubler F, Douglas R. A Framework for Modeling the Growth and Development of Neurons and Networks. Front Comput Neurosci [Internet]. 2009 Nov 20 [cited 2019 Mar 29];3. Available from: https://www.ncbi.nlm.nih.gov/pmc/articles/PMC2784082/

8. Buettner HM. Nerve growth dynamics. Quantitative models for nerve development and regeneration. Annals of the New York Academy of Sciences. 1994;745:210–21.

9. Holmquist B, Kanje M, Kerns JM, Danielsen N. A mathematical model for regeneration rate and initial delay following surgical repair of peripheral nerves. Journal of neuroscience methods. 1993;48(1–2):27–33.

10. Podhajsky RJ, Myers RR. A diffusion-reaction model of nerve regeneration. Journal of neuroscience methods. 1995;60(1–2):79–88.

11. Tse THZ, Chan BP, Chan CM, Lam J. Mathematical modeling of guided neurite extension in an engineered conduit with multiple concentration gradients of nerve growth factor (NGF). Annals of biomedical engineering. 2007;35(9):1561–72.

12. Georgiou M, Bunting SCJ, Davies HA, Loughlin AJ, Golding JP, Phillips JB. Engineered neural tissue for peripheral nerve repair. Biomaterials. 2013 Oct 1;34(30):7335–43.

13. Carvalho CR, Oliveira JM, Reis RL. Modern Trends for Peripheral Nerve Repair and Regeneration: Beyond the Hollow Nerve Guidance Conduit. Front Bioeng Biotechnol [Internet]. 2019 [cited 2020 Feb 7];7. Available from: https://www.frontiersin.org/articles/10.3389/fbioe.2019.00337/full

14. O'Rourke C, Day AGE, Murray-Dunning C, Thanabalasundaram L, Cowan J, Stevanato L, et al. An allogeneic 'off the shelf'therapeutic strategy for peripheral nerve

tissue engineering using clinical grade human neural stem cells. Scientific reports. 2018;8(1):2951.

15. Kim Y-P, Lee G-S, Kim J-W, Kim MS, Ahn H-S, Lim J-Y, et al. Phosphate glass fibres promote neurite outgrowth and early regeneration in a peripheral nerve injury model. Journal of tissue engineering and regenerative medicine. 2015;9(3):236–46.

16. Coy R, Al-Badri G, Kayal C, O'Rourke C, Kingham PJ, Phillips JB, et al. Combining *in silico* and *in vitro* models to inform cell seeding strategies in tissue engineering. J R Soc Interface. 2020 Mar;17(164):20190801.

17. Codling EA, Plank MJ, Benhamou S. Random walk models in biology. Journal of The Royal Society Interface. 2008 Aug 6;5(25):813–34.

18. Stefanoni F, Ventre M, Mollica F, Netti PA. A numerical model for durotaxis. J Theor Biol. 2011 Jul 7;280(1):150–8.

19. Dickinson RB, Tranquillo RT. A stochastic model for adhesion-mediated cell random motility and haptotaxis. Journal of mathematical biology. 1993;31(6):563–600.

20. Smith JT, Tomfohr JK, Wells MC, Beebe TP, Kepler TB, Reichert WM. Measurement of cell migration on surface-bound fibronectin gradients. Langmuir. 2004;20(19):8279–86.

21. Stokes CL, Lauffenburger DA. Analysis of the roles of microvessel endothelial cell random motility and chemotaxis in angiogenesis. Journal of theoretical biology. 1991;152(3):377–403.

22. Tranquillo RT, Lauffenburger DA. Stochastic model of leukocyte chemosensory movement. Journal of mathematical biology. 1987;25(3):229–62.

23. Schienbein M, Gruler H. Langevin equation, Fokker-Planck equation and cell migration. Bulletin of Mathematical Biology. 1993;55(3):585–608.

24. Aeschlimann M. Biophysical models of axonal pathfinding. [Lausanne]: UNIL; 2000.

25. Segev R, Ben-Jacob E. Generic modeling of chemotactic based self-wiring of neural networks. Neural Networks. 2000;13(2):185–99.

26. Georgiou, Melanie. Development of a tissue engineered implantable device for the surgical repair of the peripheral nervous system. 2013 [cited 2020 Sep 18]; Available from: http://oro.open.ac.uk/id/eprint/61175

27. Malik AA, Gerlee P. Mathematical modelling of cell migration: stiffness dependent jump rates result in durotaxis. Journal of mathematical biology. 2019;78(7):2289–315.

28. Harland B, Walcott S, Sun SX. Adhesion dynamics and durotaxis in migrating cells. Physical biology. 2011;8(1):015011.

29. Kim M-C, Kim C, Wood L, Neal D, Kamm RD, Asada HH. Integrating focal adhesion dynamics, cytoskeleton remodeling, and actin motor activity for predicting cell migration on 3D curved surfaces of the extracellular matrix. Integrative Biology. 2012;4(11):1386–97.

30. Kim M-C, Whisler J, Silberberg YR, Kamm RD, Asada HH. Cell invasion dynamics into a three dimensional extracellular matrix fibre network. PLoS computational biology. 2015;11(10):e1004535.

31. Schwarz US, Bischofs IB. Physical determinants of cell organization in soft media. Medical engineering & physics. 2005;27(9):763–72.

32. van Oers RF, Rens EG, LaValley DJ, Reinhart-King CA, Merks RM. Mechanical cell-matrix feedback explains pairwise and collective endothelial cell behavior in vitro. PLoS computational biology. 2014;10(8):e1003774.

33. Eberhart R, Kennedy J. Particle swarm optimization. In: Proceedings of the IEEE international conference on neural networks. Citeseer; 1995. p. 1942–8.

34. Pianosi F, Wagener T. A simple and efficient method for global sensitivity analysis based on cumulative distribution functions. Environmental Modelling & Software. 2015;67:1–11.

35. Campolongo F, Braddock R. Sensitivity analysis of the IMAGE Greenhouse model. Environmental modelling & software. 1999;14(4):275–82.

36. Puy A, Piano SL, Saltelli A. A sensitivity analysis of the PAWN sensitivity index. arXiv preprint arXiv:190404488. 2019;

37. Kulraj Bhangra. Delivery and Integration of Engineered Neural Tissue [PhD thesis]. 2019.

38. Razetti A, Medioni C, Malandain G, Besse F, Descombes X. A stochastic framework to model axon interactions within growing neuronal populations. PLoS computational biology. 2018;14(12):e1006627.